ACS APPLIED MATERIALS & INTERFACES

Research Article

www.acsami.org

Multiply Twinned AgNi Alloy Nanoparticles as Highly Active Catalyst for Multiple Reduction and Degradation Reactions

Mukesh Kumar and Sasanka Deka*

Department of Chemistry, University of Delhi, North Campus, Delhi 110007, India

Supporting Information

ABSTRACT: Size dependent surface characteristics of nanoparticles lead to use of these nanomaterials in many technologically important fields, including the field of catalysis. Here $Ag_{1-x}Ni_x$ bimetallic alloy nanoparticles have been developed having a 5-fold twinned morphology, which could be considered as an important alloy because of their excellent and unique catalytic and magnetic properties. Alloying between Ag and Ni atoms on a nanoscale has been confirmed with detailed X-ray diffraction, high resolution transmission electron microscopy, energy-dispersive X-ray analysis, X-ray photoelectron spectroscopy, and magnetization measurements. Although introduced for the first time as a catalyst due to having high active surface sites, the as-synthesized nanoparticles showed one of the best multiple catalytic activity in the industrially important (electro)-catalytic reduction of 4-nitrophenol (4-NP) and 4-nitroaniline (4-NA) to corresponding amines with noticeable reduced reaction time and increased rate constant without the use of any large area support. Additionally the same catalyst showed enhanced catalytic activity in degradation of environment polluting dye molecules. The highest ever activity parameter we report here for $Ag_{0.6}Ni_{0.4}$ composition is 156 $s^{-1}g^{-1}$ with an apparent rate constant of 31.1 × 10^{-3} s^{-1} in a 4-NP reduction reaction where the amount of catalyst used was 0.2 mg and the time taken for complete conversion of 4-NP to 4-aminophenol was 60 s. Similarly, an incredible reaction rate constant (115 s^{-1}) and activity parameter (576.6 $s^{-1}g^{-1}$) were observed for the catalytic degradation of methyl orange dye where 15 s is the maximum time for complete degradation of the dye molecules. The high catalytic performance of present AgNi alloy NPs over the other catalysts has been attributed to size, structural (twinned defect) and electronic effects. This study may lead to use of these bimetallic nanostructures with excellent recyclable catalytic efficiency in many more applications.

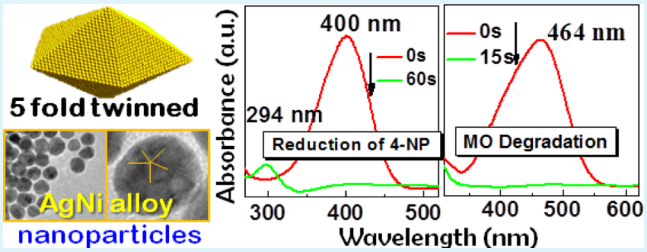

KEYWORDS: *alloy nanoparticle, AgNi, catalyst, reduction/degradation reaction, 4-nitrophenol*

1. INTRODUCTION

Bimetallic alloy nanoparticles (NPs) have recently attracted considerable attention because of their excellent and unique catalytic, electronic, optical, and magnetic properties. The corresponding potential applications of alloy NPs includes many fields such as catalyst in fuel cell and organic synthesis, oxygen reduction reactions, magnetic recording, antibacterial activity, etc.[1−4] $Ag_{1-x}Ni_x$ alloy NPs are one of the new additions to the family of alloy particles that have recently drawn attention for their unique kinds of synthesis (complete immiscibility of metals, lower surface energy of Ag, and 14% lattice mismatch) and theoretical calculations.[5−7] Other interesting aspects of these kinds of alloy NPs is from the combined strong surface plasmon resonance (SPR) of Ag in the visible spectral region due to the coherent motion of conduction band electrons against the lower electrochemical reduction potential of Ni and size dependent intrinsic ferro/superparamagnetism. A strong synergistic effect[8] could be expected from the strong coupling of noble metal based and magnetic transition metal based properties in the case of $Ag_{1-x}Ni_x$ NPs. Thus, one can expect enhanced catalytic properties of AgNi alloy NPs, because of a bifunctional reaction mechanism of bimetallic alloy electrocatalysts.

In the available literature of the Ag−Ni system, most of the particles are found to be a phase segregated core@shell structure because of the very fast reduction potential of Ag^{1+}→Ag^0 over Ni^{2+}→Ni^0 and the thermodynamic stability. In these phase segregated core@shell systems, either one of the metals is the core and the other is the shell with assorted morphologies and sizes for catalytic and biological applications.[9−12] However, complete immiscibility, the lower surface energy of Ag, and the 14% lattice mismatch between the two metals have been overcome in recent years by only a few researchers to produce true alloy NPs employing new synthesis techniques. At the nano level, the alloying behavior is different, as the size effect plays a major role in facilitating alloy formation by changing the heat of formation from positive to negative (opposite in the case of a bulk counterpart) due to the surface energy contribution. Thus, when the particles are nanometer sized,

Received: June 23, 2014
Accepted: August 29, 2014
Published: August 29, 2014

the surface/size effect and the alloy composition favor the alloying process of the thermodynamically immiscible systems and ensure better phase stability.[13] Initially, physical methods, such as vapor quenching,[14] gas condensation,[15] and the γ-radiation technique,[5,6] have been reported for the synthesis of AgNi alloy NPs. However, chemical reduction methods have been used in recent years for the synthesis of AgNi NPs for determining particle size limits for alloy formation,[16] exploration of magnetic properties,[17] and for the studies on optical limiting and photonic applications, which exhibited substantial enhancement in the optical limiting efficiency.[18]

In this paper, we have reported a novel synthesis of monodispersed $Ag_{1-x}Ni_x$ multiple twinned alloy nanoparticles (MTANP) in the presence of hexadecylamine and octadecene following a high temperature colloidal reduction method. The composition of the solid solution can be tuned easily to get the desired efficient catalyst composition for multiple reduction and degradation reactions. Detailed X-ray diffraction (XRD), high resolution transmission electron microscopy (HRTEM), energy dispersive X-ray analysis (EDAX), selected area electron diffraction (SAED), and X-ray photoelectron spectroscopy (XPS) studies revealed the alloying of Ag and Ni metals in the respective compositions and ruled out the formation of phase segregated core/shell particles. The entire alloy NPs series is found to be weakly magnetic, where order of magnetization increases with the increasing amount of incorporated Ni into Ag lattice. As-synthesized $Ag_{1-x}Ni_x$ alloy NPs are examined as possible candidates of catalysts for the reduction of various nitro-aromatic compounds and degradation of organic dye molecules. Nitro-aromatic compounds, for instance, 4-nitrophenol (4-NP) and 4-nitroaniline (4-NA), are important commercial compounds have significant functions in many industries such as the production of anilines, agrochemicals, explosives, pharmaceuticals, dyes, etc.[19,20] These compounds are important intermediates for the manufacture of analgesic and antipyretic drugs such as acetaminophenol, acetanilide, paracetamol, and phenacetin. However, at the same time, these nitro-aromatic compounds are found to be environmentally poisonous materials and a major class of aquatic contaminants.[21,22] The nitro-aromatic pesticides are hydrophobic contaminants that can accumulate in sediments by the deposition of suspended solids from surface waters. 4-NP was reported as a potential carcinogen, teratogen, and mutagen; accordingly, many aromatic nitrocompounds have been included in environmental legislation.[23] Hence, to reduce these compounds to beneficial amines and to decompose these harmful organic dyes, various nanomaterials have been developed as catalysts and reported so far. However, among the various reports on variety of catalysts[12,24−29] with maximum catalytic activity, we found that our as-synthesized $Ag_{0.6}Ni_{0.4}$ alloy NP showed the best catalytic activity (activity parameter $K = 156\ s^{-1}\ g^{-1}$) for the reduction of 4-NP to 4-AP and also showed a very high degradation rate for the catalytic degradation of methyl orange and Rhodamine B dyes. In addition, we found the requirement of very small amount of present multiple twinned nanoparticle reusable catalyst for the very fast reduction and degradation reaction.

2. EXPERIMENTAL SECTION

2.1. Materials. Nickel acetate tetrahydrate ($Ni(OCOCH_3)_2{\cdot}4H_2O$, 99.9%), hexadecylamine (HDA, 98%), 1-octadecene (ODE, 90%,), oleylamine (OLA, 90%), and Rhodamine B dye (RhB, 97%) were from Sigma-Aldrich, USA. Trioctylphosphene (TOP, 98%) was from Strem Chemicals, USA. Nickel nitrate hexahydrate ($Ni(NO_3)_2.6H_2O$), sodium borohydrid ($NaBH_4$, 95%), and methyl orange dye (MO) were from Merck, India. Silver nitrate ($AgNO_3$, 99.9%), Rankem analytical reagent, 4-nitrophenol (4-NP, 99%), and 4-nitroaniline (4-NA, 99%) were from Spectrochem, India. All chemicals were used as received without further purification.

2.2. Synthesis of AgNi Alloy Nanoparticles. A single pot approach was employed for the synthesis of $Ag_{1-x}Ni_x$ alloy nanoparticles with varying compositions, where x = 0, 0.2, 0.4, 0.5, 0.6, 0.8, and 1.0. Typically, $NiNO_3{\cdot}6H_2O$ (0.2−0.8 mmol), $AgNO_3$ (0.8−0.2 mmol), and HDA (1.5 mmol) were added to 8 mL of ODE in a three necked round-bottom flask equipped with condenser, temperature controller, and magnetic stirring bar. The reaction mixture was stirred and degassed at 110 °C for 30 min. After that, the reaction mixture was brought to 250 °C and kept at this temperature for 40 min under a continuous flow of N_2. During the synthesis of different compositions of AgNi alloy NPs, the total amount of both metal precursors was kept at 1.0 mmol. After the reaction, the mixture was cooled to room temperature naturally and the product was purified by precipitation with ethanol. The as-obtained dark brown precipitate was centrifuged and washed with ethanol for three times and finally dispersed in toluene for further characterizations. A fraction of the sample was dried at room temperature for the study of various catalytic activities.

2.3. Synthesis of Ag Nanoparticles. Ag NPs were synthesized by the same method as discussed above. In this synthesis, 1 mmol $AgNO_3$ was used without the addition of any Ni metal precursor while other parameters were kept constant. A fraction of the sample was dried at room temperature for the study of various catalytic activities.

2.4. Synthesis of Ni Nanoparticles. Nickel NPs could not be formed following the above approach when x = 1, hence Ni NPs were separately synthesized following a reported method with minor modifications.[30] 2 mmol $Ni(OCOCH_3)_2{\cdot}4H_2O$ was added to 16 mmol OLA in a three necked round-bottom flask and degassed at 100 °C for 30 min. 1.6 mmol TOP was injected to the reaction mixture under continuous N_2 flow. The reaction mixture was brought to 220 °C and stirred at this temperature for 2 h. After the reaction, the product was precipitated and washed with ethanol and finally dispersed in toluene.

2.5. Sample Characterization. The crystal structure and purity of as-synthesized alloy NPs, Ag, and Ni NPs were characterized by powder X-ray diffraction (XRD) patterns recorded on a Bruker D8 Advance X-ray diffractometer by using Cu Kα as a radiation source at room temperature. Transmission electron microscopy (TEM), high resolution TEM (HRTEM), and selected area electron diffraction (SAED) images were obtained from a Philips Technai $G^2$30 transmission electron microscope operating at an accelerating voltage of 200 kV equipped with an energy dispersive X-ray spectroscopy (EDAX) attachment. TEM samples were made by putting a drop of sample dispersion in toluene on a carbon coated copper grid and letting the solvent evaporate. Elemental proportions in the as-synthesized alloy samples were analyzed using a Zeenit 700p Analytik Jena atomic absorption spectrometer (AAS). The surface phase compositions of the films were analyzed by means of X-ray photoelectron spectroscopy (XPS, SPECS XPS system). The base pressure in the main chamber was $\leq 10^{-9}$ mbar and the photoelectrons were excited using a Mg Kα energy source of 1253.6 eV. The data acquired has a resolution of 0.1 eV and the accuracy in binding energy determination was 0.05 eV. The C 1s (284.6 eV) peak was considered as a reference. Optical absorption measurements were carried on a PerkinElmer LAMBDA 35 spectrophotometer. Magnetic properties of the nanoparticle samples were characterized by a vibrating sample magnetometer (MicroSense EV9) at room temperature (23 °C).

2.6. Catalytic Study. *2.6.1. Catalytic Reduction of Nitro Compounds.* For evaluating the activity of our AgNi alloy NPs as an efficient catalyst, the reductions of 4-NP and 4-NA were chosen as model reactions. Catalytic reduction reaction study of 4-NP and 4-NA was carried out in a fashion as discussed below. In a typical process, 2.5 mL of aqueous solution of nitro compound (0.2−1.0 mM) and 0.3 mL of 0.2 M $NaBH_4$ were taken in a standard quartz cuvette of 1 cm path length and 3 mL volume. Following which, 100 μL aqueous solution of

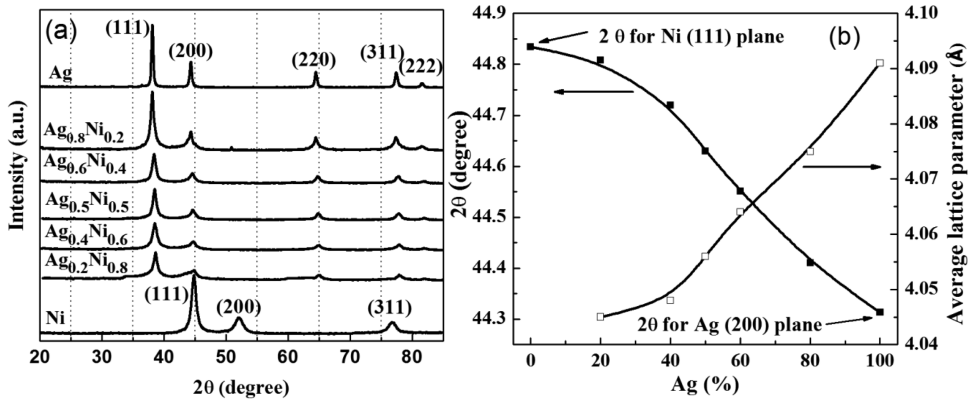

Figure 1. (a) Powder XRD patterns of as-synthesized Ag, Ni, and AgNi alloy NPs with variable elemental ratios showing the *fcc* structure. (b) Composition dependent diffraction angle at the (200) plane of Ag within the 2θ range 44.31−44.83°. Right axis: average lattice parameter (a, Å) vs amount of Ag content.

homogeneously dispersed AgNi (0.2 mg, 2 mg/mL) nanocatalyst was added in the same cuvette and optical absorption spectra (UV−vis region) were recorded immediately against time at room temperature (23 ± 1 °C). A similar scheme was applied for all nanocatalyst ($Ag_{1-x}Ni_x$, x = 0, 0.2, 0.4, 0.5, 0.6, 0.8, and 1.0) samples. For studying the effect of catalyst dose, the amount of AgNi catalyst was varied (0.2−0.5 mg); however, volume and concentration of 4-NP and $NaBH_4$ were kept constant (2.5 mL of 0.2 mM and 0.3 mL of 0.2 M, respectively). In a similar way, 4-NP concentration was varied (0.2−1.0 mM), however, keeping other parameters constant (0.2 mg of AgNi catalyst and 0.3 mL of 0.2 M $NaBH_4$) for studying concentration effect of the substrate.

2.6.2. Catalytic Degradation of Dyes. For measuring dye degradation activity of a catalyst, we have chosen MO and RhB dyes as the standard and $Ag_{0.6}Ni_{0.4}$ alloy NPs as the catalyst (found most active composition from nitro compound reduction reactions). In this process, 2.5 mL of aqueous solution of dye (2×10^{-5} M) and 0.3 mL of 0.2 M $NaBH_4$ were placed in a quartz cuvette. Following this, 100 μL of aqueous solution containing 0.2 mg of catalyst was added to the above solution in the cuvette and UV−vis spectra against time were recorded. For investigating the effect of catalyst dose on reaction rate, the amount of catalyst was varied from 0.2 to 0.5 mg; however, other parameters for dye and $NaBH_4$ were kept constant (2.5 mL of 1×10^{-4} M MO and 0.3 mL of 0.2 M $NaBH_4$). To check the effect of concentration of dye on the rate of reaction, the concentration of MO was varied from 0.2 to 1.0×10^{-4} M; however, the amounts of catalyst and $NaBH_4$ were kept constant (0.2 mg and 0.3 mL of 0.2 M, respectively).

3. RESULTS AND DISCUSSION

3.1. Structural, Morphological, Surface and Magnetic Characterizations. Phase purity and composition of the different alloy NPs were examined by powder XRD measurements. Figure 1a represents the XRD patterns of as synthesized Ag, Ni, and AgNi alloy NPs. These patterns clearly revealed the *fcc* structure of all the samples. For Ag NPs, five characteristic peaks corresponding to the (111), (200), (220), (311), and (222) planes of the *fcc* structure were obtained at 2θ diffraction angles of 38.14, 44.31, 64.49, 77.42, and 81.60°, respectively (JCPDS No. 04-0783). For Ni NPs, peaks corresponding to (111), (200), and (311) were observed at 44.83, 52.15, and 76.90° (JCPDS No. 04-0850). However, interesting features have been observed in the case of powder XRD patterns of AgNi alloy NPs. All the alloy compositions showed five peaks resembling the (111), (200), (220), (311), and (222) planes of Ag but with slight deviation from the actual 2θ values. As the amount of Ni content increases, the (111) plane of Ag is shifted toward higher 2θ values. Moreover, the (200) peak of Ag started disappearing with increasing content of Ni and finally a well resolved peak at 44.83° appeared for Ni(111). Similar decreases in the intensity of the peaks with increasing amounts of Ni content in the alloys were observed for the Ag(220) and Ag(311) peaks, which were not observed in the case of reported Ag/Ni core/shell systems.[9−12] A magnified 2θ range elaborating the peak position shifting and changing of peak intensity with Ag/Ni contents is shown in Figure S1 (Supporting Information). In the literature for Ag/Ni core/shell NPs[10,12,31] and Ni NPs,[32,33] along with other planes, the (200) plane of *fcc* Ni at 52.15° is prominent, confirming the presence of nickel in its intact state. However, in the present alloy NPs, an XRD peak at 52.15°, corresponding to the (200) plane of *fcc* Ni was not found, concluding that no Ni NPs were formed heterogeneously. This observation is consistent with other AgNi alloy particles synthesized using different methods.[17,18] Absence of characteristic peak of Ni and resemblance with Ag *fcc* structure confirmed the formation of solid solution in which Ni atoms are present in Ag matrix.[34]

As stated above, an increase in diffraction angle was observed with increasing Ni content in all alloy compositions and this shift in diffraction angle with respect to the Ag(200)/Ni(111) planes is shown in Figure 1b. From this figure, it was noted that the diffraction angle of all alloy samples was between 2θ values of the (200) plane of Ag and the (111) plane of Ni. This further supports the formation of homogeneous solution of metals according to Vegard's law. From XRD refinements, interplanar spacing (d_{hkl}) and average lattice parameter (a, Å) was calculated for all the samples and the data are entered in Table 1. Moreover, the change in calculated lattice parameter with the $Ag_{1-x}Ni_x$ composition variation is plotted in Figure 1b in the right axis. From these data, decrease in lattice constant or d-spacing was observed which was due to incorporation of small sized Ni atoms (124 pm) in Ag (144 pm) matrix.

The size, morphology, and crystal structure of alloy NPs were further examined by transmission electron microscopy (TEM) and high resolution transmission electron microscopy (HRTEM). Figure 2a−c represents the low magnified TEM images of Ag, $Ag_{0.6}Ni_{0.4}$ and $Ag_{0.2}Ni_{0.8}$ compositions, respectively. These TEM images mainly show the presence of multiple twinned nanostructures that looks spherical at low magnifications. The average particle sizes in the case of $Ag_{0.6}Ni_{0.4}$ and $Ag_{0.2}Ni_{0.8}$ compositions are found to be similar, ∼19 nm (see Figure S2, Supporting Information, for particle

Table 1. Alloy Compositions, *d*-Spacing and Calculated Average Lattice Constant (*a*) Values from Powder XRD Analyses

sample compositions	peaks (*hkl*) 111 d (Å)	200 d (Å)	220 d (Å)	311 d (Å)	average lattice constant (Å)
Ag	2.375	2.043	1.444	1.231	4.091
$Ag_{0.8}Ni_{0.2}$	2.349	2.037	1.443	1.230	4.075
$Ag_{0.6}Ni_{0.4}$	2.342	2.032	1.438	1.227	4.064
$Ag_{0.5}Ni_{0.5}$	2.336	2.025	1.436	1.226	4.056
$Ag_{0.4}Ni_{0.6}$	2.332	2.022	1.435	1.224	4.048
$Ag_{0.2}Ni_{0.8}$	2.325	2.021	1.434	1.223	4.045

size distribution histograms of three compositions), however, a little smaller for Ag particles where the nanoparticles diameter was found to be ~14 nm. For further study, HRTEM images were taken (Figure 2d,e), which clearly shows 5-fold twinned nanostructures and the presence of clear lattice fringes. HRTEM results show the presence of twinned nanostructures oriented in different directions in which primarily five crystalline domains separated with twinned boundary (more images in Figure S3, Supporting Information). The *d*-spacing calculated from lattice fringes of adjacent faces was 0.24 nm, which is consistent with the (111) plane of Ag−Ni alloy NPs. Furthermore, we have considered a single crystal $Ag_{0.6}Ni_{0.4}$ particle and further magnified the defect free area (see Figure 2f) for the confirmation of orientation of Ag and Ni planes in an alloy system, and to exclude the possibility of formation of phase segregated core/shell system. As reported earlier by Zhang et al.[5,6] for *fcc* AgNi twinned particles and by Tsen et al.[35] for *fcc* Au twinned particles, a similar trend has been observed in the present case. The experimental results suggest a lattice spacing of 0.23 and 0.24 nm and the dihedral angle between these two sets of fringes is 70°. All the values match well with the bulk Ag(111) Miller plane spacing of 0.236 nm and the corresponding angle of 70.5°. Moreover, it was suggested that the measured {111} fringe spacing can be either larger or smaller than the bulk value due to small crystal tilts.[36] The calculated two-dimensional fast Fourier transform (2D-FFT) pattern from panel f is shown in Figure 2g, and the results again confirmed the exposure of the (111) plane of alloy NPs. The presence of 5-fold twin boundaries and exposure of the (111) facets confirmed the decahedral structure for AgNi alloy NPs. The SAED pattern of $Ag_{0.6}Ni_{0.4}$ NPs is shown in Figure 2h. The SAED pattern represents the crystalline nature of the particles with the *fcc* structure, where the (111), (200), (220), and (311) lattice planes were clearly indexed in agreement with XRD results. The elemental analysis using energy dispersive X-ray (EDAX) spectroscopy was carried out on various samples for the study of the stoichiometry and the representative EDAX analysis of $Ag_{0.6}Ni_{0.4}$ alloy sample is shown in Figure 2i and, for $Ag_{0.2}Ni_{0.8}$, $Ag_{0.4}Ni_{0.6}$, and $Ag_{0.8}Ni_{0.2}$ alloy NPs, in Figure S4 (Supporting Information). EDAX

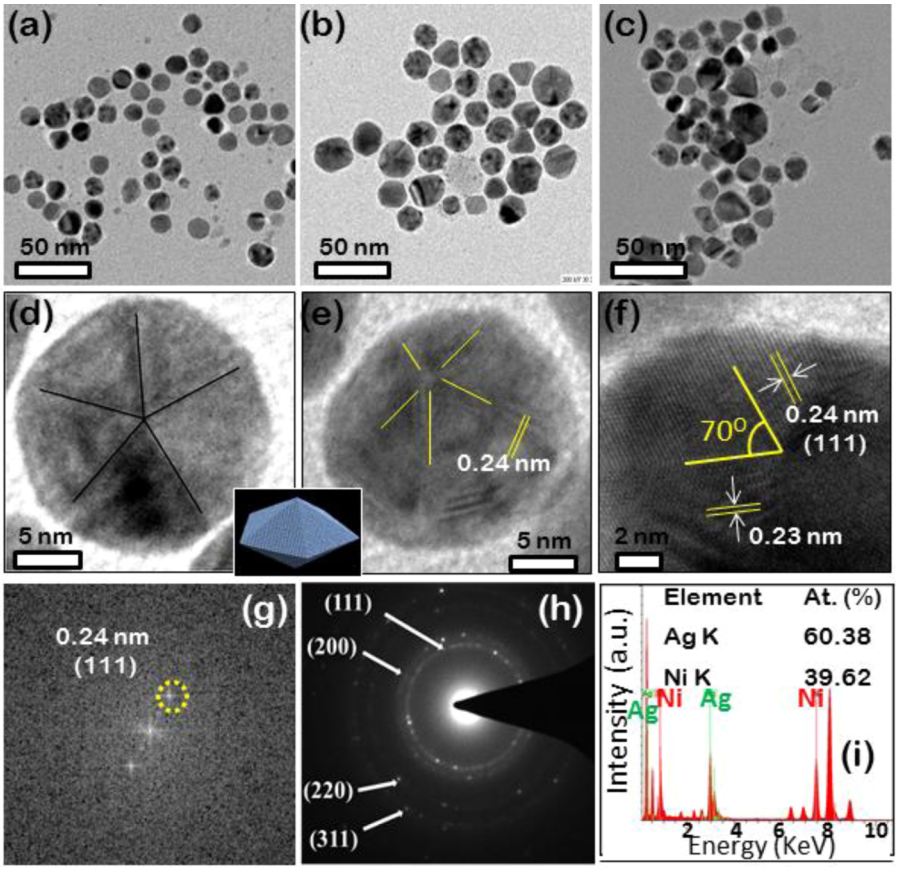

Figure 2. Low magnified electron micrograph images (a) Ag, (b) $Ag_{0.6}Ni_{0.4}$, and (c) $Ag_{0.2}Ni_{0.8}$ alloy nanoparticles. (d,e) 5-Fold multiple twinned structure under HRTEM imaging and inset: model of 5-fold twinned structure, (f) clear lattice fringes and the dihedral angle between them seen in another $Ag_{0.6}Ni_{0.4}$ alloy single NP, (g) calculated 2D-FFT pattern from the region shown in panel f. (h) SAED pattern from panel b and (i) EDAX analysis of $Ag_{0.6}Ni_{0.4}$ alloy NPs.

dx.doi.org/10.1021/am503913y | *ACS Appl. Mater. Interfaces* 2014, 6, 16071−16081

results confirmed the presence of Ag and Ni elements in alloy samples and in corresponding proportions. The composition of the Ag:Ni ratio in the present sample ($Ag_{0.6}Ni_{0.4}$) was found to be 60.38:39.62, which is consistent with the expected Ag:Ni stoichiometric elemental ratio. The compositional ratio of Ag:Ni in the other alloy particles was also found to be consistent with the corresponding stoichiometric elemental ratio from the EDAX analyses. Further, we have carried out atomic absorption spectroscopic (AAS) measurements to determine the elemental ratio of the as-synthesized alloy samples. In all cases, compositional ratios of Ag:Ni were found to be consistent with the corresponding stoichiometric elemental ratio according to synthesis and the ratios obtained from EDAX measurements.

Alloy and Twinned Particle Formation Mechanism. The facile synthesis of AgNi alloy MTANPs was carried out in ODE, where HDA acts as a surfactant and weak reducing agent. From controlled experiments, it was found that Ni NPs were not formed in the absence of a Ag precursor; however, addition of $AgNO_3$ to a Ni precursor resulted into the formation of alloy NPs. This experimental observation indicated that the Ag precursor plays a crucial role in the nucleation of Ni. Because the redox pair potential of Ag^+/Ag (0.8 V) is higher than that of Ni^{2+}/Ni (−0.246 V), Ag nucleation started in the initial phase. These in situ formed Ag nuclei further induce the reduction of Ni^{2+}/Ni by the electron transfer process, as shown below

$$2Ag^0 + Ni^{2+} \rightarrow 2Ag^+ + Ni^0 \quad (1)$$

$$Ag^+ + e^- \rightarrow Ag^0 \quad (2)$$

This type of electron transfer process might cause simultaneous nucleation of both Ag and Ni within the reaction mixture, which later on grows as AgNi alloy NPs. Because HDA is a weak reducing agent that causes a slow nucleation rate, prevents separate Ni nucleation and results in a product with high anisotropy. The *fcc* metals like Ag and Au readily form a twinned nanostructure due to low twinning energy, which can compensate the strain induced by formation of completely (111) bounded NPs.[37] As indicated above (Figure 2a−e), the average size of Ag and $Ag_{0.6}Ni_{0.4}$ alloy MTANPs was ∼14 and ∼19 nm, respectively, hence larger sized AgNi alloy NPs are indicative of more stability of alloy NPs over pure Ag nanocrystals. This gain in stability might be due to incorporation of small sized Ni atoms in the Ag lattice, which lowers the bulk strain of twinned Ag lattice and this decrease in lattice strains favors the formation of a twinned alloy nanostructure. This is supported by literature report, where 5-fold twinning is found thermodynamically favorable at a small size for *fcc* metals like Ag and Au.[38] Therefore, the crystal lattice of AgNi MTANPs does not collapse, even if the alloyed samples grow larger than pure Ag MTNPs.[39]

Surface Characterization. Figure 3 presents X-ray photoelectron spectroscopy (XPS) data for the as-synthesized $Ag_{0.6}Ni_{0.4}$ nanocrystals. Figure 3a shows the survey spectrum of the sample confirming the presence of the 3d state of Ag and the 2p, 3s, and 3p states of Ni in their respective compositional ratios along with the O 1s and C 1s peaks. Figure 3b shows the two components of the Ag 3d spectrum. The Ag $3d_{5/2}$ and Ag $3d_{3/2}$ peaks occurring at the binding energies of 368.2 and 374.2 eV with a difference of 6.0 eV can be assigned to metallic Ag in a AgNi alloy.[17] The XPS spectra of Ni $2p_{3/2}$ and Ni $2p_{1/2}$ core levels and its satellites peaks are shown in Figure 3c. The Ni $2p_{3/2}$ and Ni $2p_{1/2}$ peaks appear at 855.2 and 873.0 eV,

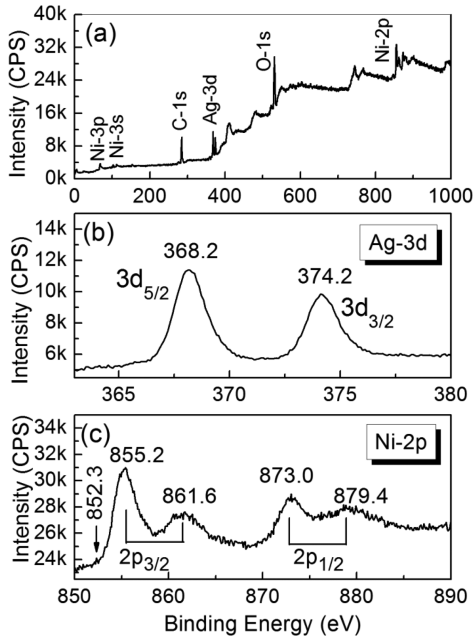

Figure 3. XPS spectra of $Ag_{0.6}Ni_{0.4}$ alloy sample. (a) Wide scan survey XPS spectrum. High resolution spectrum of (b) Ag 3d and (c) Ni 2p.

respectively, and the corresponding satellite peaks are observed at 861.6 and 879.4 eV, respectively. In both cases, the energy spacing of 17.0 eV is due to Ni^{2+}, which indicates the oxidation of a minute amount of surface Ni to NiO.[40,41] This statement is further supported by repeated XRD measurements on aged alloy samples, where no NiO peaks are observed within the diffractometer's detection limit. The peak observed at 531.3 eV, as shown in Figure 3a, can be assigned to the oxygen bonded with Ni to form some surface NiO. Further, a very weak shoulder at 852.3 eV is observed in the Ni 2p XPS spectrum, which corresponds to Ni $2p_{3/2}$ binding energy of metallic Ni.[17,40,41]

Magnetic Characterization. Magnetic properties of as-synthesized AgNi alloy NPs were studied at room temperature (23 °C) using a vibrating sample magnetometer. Figure 4 represents the magnetization curves of three compositions of AgNi alloy NPs. All the AgNi alloy samples show weak ferromagnetic behavior due to the presence of Ni atoms in the Ag lattice. The values of saturation magnetization (M_S), remanent magnetization (M_r), and coercivity (H_C) were calculated for different alloy compositions and are presented

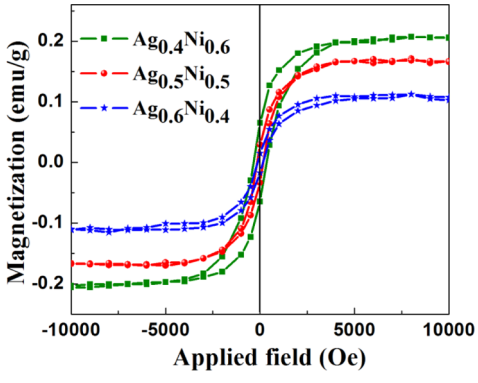

Figure 4. Magnetization of $Ag_{0.4}Ni_{0.6}$, $Ag_{0.5}Ni_{0.5}$, and $Ag_{0.6}Ni_{0.4}$ alloy NPs as a function of applied field, measured at 23 °C.

in Table 2. Magnetization data clearly shows that all three magnetic parameters (M_S, M_r, and H_C) increase with increase in

Table 2. Saturation Magnetization (M_S), Remanent Magnetization (M_r), and Coercivity (H_C) values for Different Composition of Alloy NPs

sample composition	M_S (emu/g)	M_r (emu/g)	H_C (Oe)
$Ag_{0.4}Ni_{0.6}$	0.203	0.065	349
$Ag_{0.5}Ni_{0.5}$	0.170	0.029	153
$Ag_{0.6}Ni_{0.4}$	0.111	0.015	130

Ni content. This result clearly indicates the distribution of Ni atoms in Ag lattice forming an alloy and a weak ferromagnetic interaction among the doped Ni contents in Ag lattice.

3.2. Catalytic Reduction. *Catalytic Reduction of 4-Nitrophenol.* To evaluate the catalytic performance of AgNi alloy NPs, we have chosen the catalytic reduction of 4-nitrophenol to 4-aminophenol by $NaBH_4$ as the first model reaction. The progression of the reduction reaction was monitored by UV−vis absorption spectroscopy. An aqueous solution of 4-NP is light yellow in color, which shows absorption at 317 nm. Addition of an aqueous solution of $NaBH_4$ to 4-NP results in a change of color from light yellow to deep yellow. This color change can be attributed to an increase in the alkalinity of the solution, which results in the formation of the 4-nitrophenolate ion. The 4-nitrophenolate ion shows an absorption peak at 400 nm, which remains unchanged in the presence of $NaBH_4$, even up to 30 min. This indicates the reduction process does not occur in the absence of a catalyst. This is due to presence of high kinetic barrier between the mutually repelling negative ion of borohydride (BH_4^-) and 4-nitrophenolate ion ($C_6H_4NO_3^-$).[42] As a representative case of the catalyst, after the addition of 0.2 mg of $Ag_{0.6}Ni_{0.4}$ (homogeneously dispersed aqueous solution) MTANPs, the reduction reaction is completed in 60 s. Figure 5a represents the absorption spectra of 4-NP vs time in the presence of a $Ag_{0.6}Ni_{0.4}$ nanocatalyst. From the absorption spectra, it was noted that the intensity of the absorption peak at 400 nm dramatically decreases and, at the same time, a new peak at 294 nm started to rise due to the conversion of 4-NP to 4-AP. For AgNi alloy NPs, no induction time was observed, indicating high diffusibility of reactant and product on the bimetallic surface. The optical absorption spectra show two isosbestic points at 280 and 314 nm, suggesting the formation of 4-AP as a single product. In the reduction process, the concentration of $NaBH_4$ (0.2 M) is much higher than that of 4-NP (0.2 mM) and remains almost constant during the reaction process. Considering this, first-order kinetics was applied to calculate the catalytic performance of all $Ag_{1-x}Ni_x$ alloy NPs compositions. The apparent rate constant of different alloy nanocatalyst samples including monometallic Ag and Ni NPs as controlled reactions was measured from linear plots of $\ln(A_t/A_0)$ vs reduction time (Figure 5b). Here A_t and A_0 are the absorbance of the 4-NP solution at times $t = t$ and $t = 0$, respectively, which are equivalent to the concentrations at times $t = t$ (C_t) and $t = 0$ (C_0). The apparent rate constants (k_{app}) for all samples were determined from the slope of a linear plot and are presented in Table 3.

These results clearly demonstrate the higher activity of alloy NPs over their monometallic counterparts. The $Ag_{0.6}Ni_{0.4}$ alloy sample showed the highest reaction rate (k_{app} = 31.1 × 10^{-3} s^{-1}) among all the alloy compositions, which is also nearly 4

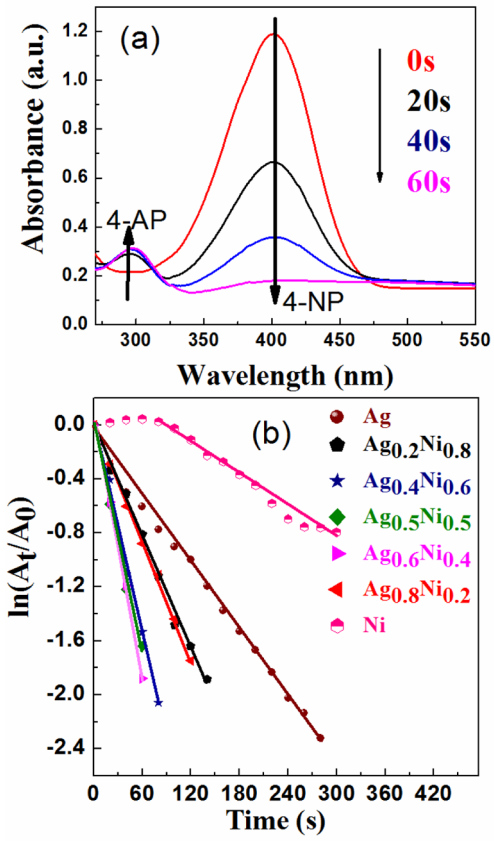

Figure 5. (a) Absorption spectra of 4-nitrophenol in the presence of 0.3 mL of 0.2 M $NaBH_4$ and 0.2 mg of $Ag_{0.6}Ni_{0.4}$ catalyst. (b) $\ln(A_t/A_0)$ vs time plot of all alloy compositions including Ag and Ni metals for first-order kinetics.

Table 3. Summary of Comparative Reduction Time (t), Apparent Rate Constant (k_{app}), and Activity Parameter (K) for Different MTANP Samples

sample name	reduction time (s)	apparent rate constant (k_{app}, 10^{-3} s^{-1})	activity parameter (K, s^{-1} g^{-1})
Ag	280	7.8	39
$Ag_{0.8}Ni_{0.2}$	80	14.4	72
$Ag_{0.6}Ni_{0.4}$	60	31.1	156
$Ag_{0.5}Ni_{0.5}$	65	28.0	140
$Ag_{0.4}Ni_{0.6}$	80	26.2	131
$Ag_{0.2}Ni_{0.8}$	140	13.7	68.5
Ni	540	4.5	22.5

times that of Ag (7.8 × 10^{-3} s^{-1}) and approximately 7 times that of Ni (4.5 × 10^{-3} s^{-1}) NPs, showing a strong synergistic effect of Ag and Ni alloying. To compare the catalytic activity of our catalyst with reported ones in literature, we calculated the activity parameter $K = k_{app}/m$, where k_{app} is a rate constant and m is mass of catalyst loaded. The activity parameters of some recently reported highly active catalyst were compared with our measured activity parameter. The high activity of our catalyst was observed as compared to a few of the best activities reported recenty for the same catalytically induced reduction reaction,[12,24−29] but using different types of alloys and their composite NPs. However, Qiao et al. and Zhang et al. separetely reported higher activity of Ag−Au and Pt−Pd alloy NPs supported on Fe_3O_4@C than the present AgNi material, where synthesis of catalyst is critical and relatively expensive

dx.doi.org/10.1021/am503913y | ACS Appl. Mater. Interfaces 2014, 6, 16071−16081

materials were used.[43,44] Because our catalyst is of low cost, easy to synthsize, and highly efficient, it is beneficial over those from other reports.

The effects of 4-NP concentration and catalytic loading were studied by choosing the highest active $Ag_{0.6}Ni_{0.4}$ alloy NPs as the primary catalyst. Figure 6a represents the absorbance vs

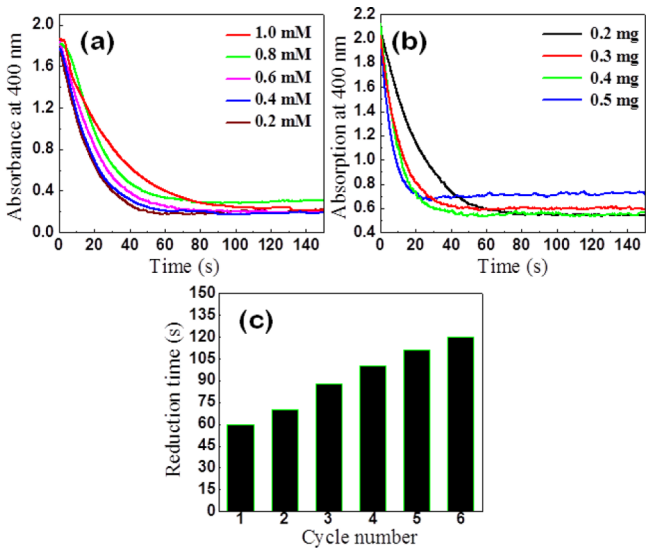

Figure 6. Absorption spectra recorded at 400 nm with 0.3 mL of 0.2 M $NaBH_4$ showing (a) effect of 4-NP concentration on reduction time with 0.2 mg $Ag_{0.6}Ni_{0.4}$ catalyst, (b) effect of catalyst loading on reduction time with 0.2 mM 4-NP. (c) Reusability of $Ag_{0.6}Ni_{0.4}$ as catalyst for reduction of 0.2 mM 4-NP with 0.3 mL of 0.2 M $NaBH_4$.

time spectra at 400 nm for different concentrations of 4-NP; however, Figure 6b represents absorbance vs time spectra at 400 nm for different catalytic loadings on reaction rate while keeping other parameters constant. The results were compared in terms of reduction time, which is inversely proportional to reaction rate. From Figure 6a, an increase in reduction time was noted with an increase in concentration of 4-NP. The reduction time for the 0.2 mM 4-NP solution was 60 s whereas 68, 79, 85, and 100 s were observed for 0.4, 0.6, 0.8, and 1.0 mM 4-NP, respectively. An increase in substrate concentration promotes more 4-NP molecules on the catalytic surface, which slows down adsorption of the BH_4^- ion. This resulted in reduced electronic communication between 4-NP and $NaBH_4$ molecules and slowed down the reaction rate. However, in the case of catalyst loading, a sharp decrease in reduction time was observed with increasing catalyst amount (Figure 6b). A 0.2 mg sample of catalyst completed reduction in 60 s whereas the reduction reaction could be completed within a record time of 20 s if 0.5 mg of catalyst was used. This is obviously due to availability of increased active catalytic surfaces, which increases with the increasing amount of catalyst.

To check the stability of an alloy catalyst, a recyclability test was carried out over six cycles using the $Ag_{0.6}Ni_{0.4}$ composition, which showed the highest catalytic activity toward 4-NP reduction (entry 3 in Table 3). After each test, the catalyst was recovered by centrifugation followed by washing with distilled water and drying. Figure 6c represents the reduction time for successive cycle. These results concluded recyclability of alloy NPs with the increase in reduction time from 60 to 120 s after six successive cycles. This increase in reduction time may be due to aggregation and catalyst lost during successive cycles.

From the analysis of UV−vis results, outstanding catalytic activity was observed for AgNi alloy NPs. The high catalytic performance of the present AgNi alloy NPs over the other reports can be attributed to following three facts: (a) size effect, availability of high effective surface area for catalysis due to small sized alloy NPs as it is well-accepted that the apparent kinetic rate constant k_{app} is proportional to the total surface (S) of metal nanoparticles;[45] (b) structural effect, structural defects created due to formation of twinned nanostructure favor the enhanced adsorption of substrates and reducing agents and enhance catalytic performance of alloy NPs; (c) electronic effect, the electronegativity difference between Ag (1.93) and Ni (1.91) metals would cause electron transfer from Ni to Ag resulting in the creation of electron rich and electron poor regions on the bimetallic surface. The existence of these regions on metallic surfaces facilitates electronic communication between adsorbed molecules, which could enhance the adsorption capability of alloy NPs. Hence alloying of Ag and Ni would cause higher uptake and increased electron transfer between substrate molecules resulting in high catalytic activity of alloy NPs. Notwithstanding, it is not clear to us yet why the $Ag_{0.6}Ni_{0.4}$ composition is more active than the other compositions. It might be the last point from above, where 60% Ag and 40% Ni and the effective electronegativity[46] play a balancing role for the best electron transfer from BH_4^- to substrate due the electronic effect. Because noble metals are considered for high catalytic activity, owing to their stability, recyclability, and high electronic conduction, as compared to transition metals, in the present case, the catalytic activity of Ag is approximately double that of pure Ni (Table 3). However, in the case of alloy systems, both the electronegativity difference and synergistic effects of individual metals play the major role in determining the final property of the former. Therefore, alloy NPs show higher catalytic activity than the pure metal (Ag, Ni) NPs; however, at the same time, $Ag_{0.6}Ni_{0.4}$, $Ag_{0.5}Ni_{0.5}$, and $Ag_{0.4}Ni_{0.6}$ alloy NPs show comparatively higher activity (i.e., 156, 140, and 131 $s^{-1}g^{-1}$, respectively) than the rest. The minor decrease in activity for $Ag_{0.5}Ni_{0.5}$ and $Ag_{0.4}Ni_{0.6}$ may be attributed to the lower content of Ag. Because the activity of $Ag_{0.8}Ni_{0.2}$ and $Ag_{0.2}Ni_{0.8}$ is distinctively less than the others, this may be due to the large difference in Ag:Ni ratios, resulting in a very weak synergistic effect. In other words, it can be stated that the synergistic effect plays a maximum role when the differences in the ratios of Ag and Ni are small. Thus, the highest activity of $Ag_{0.6}Ni_{0.4}$ is likely to be from the best combined effect of both factors (high electronic conduction due to balanced Ag content and strong synergistic effect resulting from Ag and Ni combination). On the basis of the above facts (a−c), a schematic illustration is demonstrated in Figure 7 showing the catalytic reaction mechanism of the reduction of 4-NP to 4-AP with an aqueous solution of $NaBH_4$ over a AgNi alloy NP catalyst.

Catalytic Reduction of 4-Nitroaniline. Apart from 4-NP, we examined the catalytic activity of the $Ag_{0.6}Ni_{0.4}$ alloy nanocatalyst for the reduction of 4-nitroaniline (4-NA). Absorption spectra for catalytic reduction of 4-NA by $NaBH_4$ in the presence of 0.2 mg of catalyst are shown in Figure 8a. 4-NA exhibits an absorption peak at 380 nm, which gradually decreases in intensity after addition of the AgNi nanocatalyst and disappears in 80 s. Within that same time, two peaks at 240 and 300 nm were observed, attributed to the formation of *p*-phenylenediamine.[16] The rate of reaction was measured by applying first-order kinetics as discussed in 4-NP reduction.

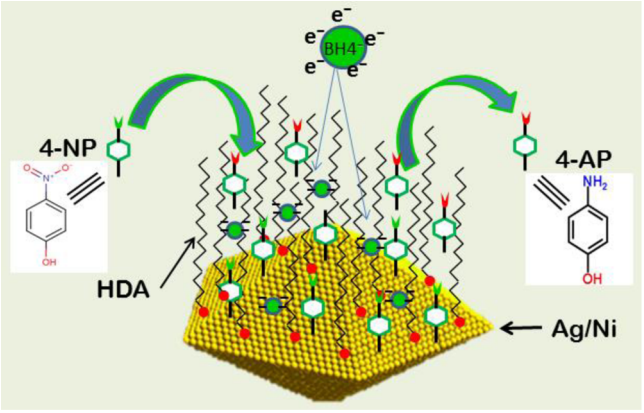

Figure 7. Schematic illustration demonstrating the catalytic reaction mechanism of the reduction of 4-NP to 4-AP by aqueous solution of $NaBH_4$ over AgNi alloy NP catalyst.

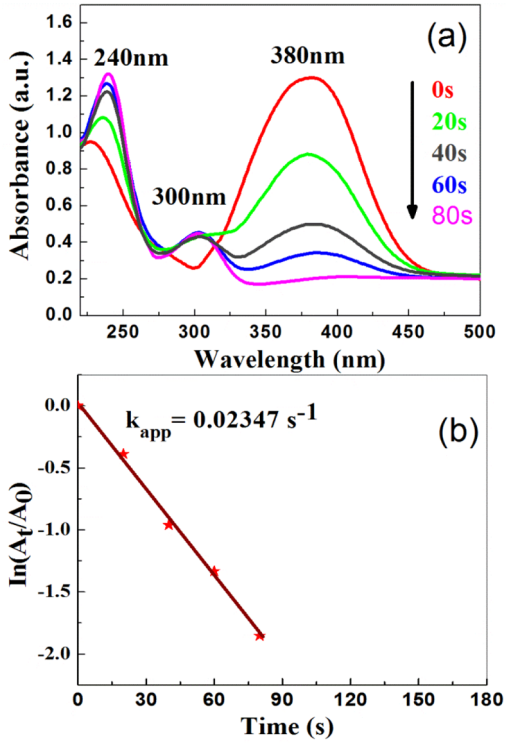

Figure 8. (a) Absorption spectra of 0.2 mM 4-nitroaniline in the presence of $NaBH_4$ (0.3 mL of 0.2 M) and 0.2 mg $Ag_{0.6}Ni_{0.4}$ nanocatalyst. (b) Plot of $\ln(A_t/A_0)$ vs time representing first order kinetics for the reduction reaction of 4-nitroaniline.

The apparent rate constant calculated by plotting $\ln(A_t/A_0)$ vs time (Figure 8b) for 4-NA reduction was found to be 23.5×10^{-3} s^{-1}, which is slightly lower than the 4-NP reduction rate for the same catalyst composition. This difference in rate is due to presence of different substituents on nitrobenzene, which varies the activation energy for catalytic reduction reaction.

3.3. Catalytic Degradation of Dyes. Organic dyes such as methyl orange, Rhodamine B, methyl red, Eosin Y, etc., which are generally used in dye industries and biological tagging, cause adverse effects on our environment, so their degradation is necessary before discharging them to aquatic environments. In this report, we choose MO and RhB dyes, for investigating model degradation activity of the as-synthesized AgNi catalyst. The degradation reaction of dyes was studied by adding $NaBH_4$ to an aqueous solution of dyes in the presence of AgNi catalyst and reaction kinetics was monitored by measuring optical absorption against time in an UV−vis spectrometer.

Catalytic Degradation of Methyl Orange. Figure 9a represents the absorption spectra of the degradation of MO by $NaBH_4$ in the presence of AgNi catalyst. From this spectrum, it was observed that MO exhibits a characteristic absorption peak at 464 nm[17], which disappears just in 15 s after adding the catalyst, showing a high catalytic activity. When the experiment was carried out in the absence of the AgNi catalyst, it was observed that $NaBH_4$ showed almost zero activity over a period of 210 min (Figure 9b). Thus, it can be corroborated that the catalyst is providing a surface for the adsorption of both species (substrate dye and $NaBH_4$ reducing agent molecules), which increases the rate of degradation reaction by increasing electron transfer between these reacting molecules. In the present reaction, $NaBH_4$ concentration was very high, which remained almost unchanged during the course of reaction. So, first-order kinetics was applied for studying reaction kinetics. The apparent rate constant was calculated from the linear plots of $\ln(A_t/A_0)$ against time, as discussed in the preceding section, and the values are given in Table 4. The apparent rate constant observed for the degradation of 0.02 mM MO in the presence of 0.2 mg of catalyst was found to be 0.115 s^{-1}, which is the highest MO degradation ability and best rate constant value (fastest degradation) observed to-date in the literature,[47,48] as per our knowledge. To further gain insight, the effect of concentration of MO and catalyst loading on rate of reaction was studied while keeping the other parameters constant (Figure 9c,d). As expected, the degradation of this dye could be completed within no time by increasing the amount of catalyst two times. For comparing these results, the activity parameter (K, $s^{-1}g^{-1}$) was calculated and is presented in Table 4. From these results, it was observed that the rate of reaction decreases with increasing concentration of MO, which supports first-order kinetics of the degradation process. This decrease in rate is due to the slowing down of the electron transfer process on the catalyst surface between $NaBH_4$ and dye molecules. However, with increases in catalyst loading, increases in the rate of reaction as well as increases in the activity parameter were observed, which is obvious due to increases in the effective catalytic surface area for the degradation reaction.

Catalytic Degradation of Rhodamine B. RhB exhibits a characteristic absorption peak at 554 nm. Figure 9e represents the UV−vis degradation spectra of 0.02 mM RhB with 0.2 mg of $Ag_{0.6}Ni_{0.4}$ nanocatalyst. The absorption peak of RhB at 554 nm disappeared within 20 s in the presence of $NABH_4$ and catalyst, again showing the high activity of our catalyst. The apparent rate constant was calculated for 0.1 mM RhB from a linear plot of $\ln(A_t/A_0)$ vs time, shown as the inset in Figure 9f. The rate constant for degradation of RhB was found to be 3.63×10^{-2} s^{-1}. The high catalytic degradation activity of our catalyst can be explained on the basis of size, structural, and electronic effects, which we had already discussed in 4-NP reduction.

4. CONCLUSIONS

We have developed a colloidal high temperature based reduction reaction to synthesize multiple twinned AgNi alloy nanoparticles. At the bulk state, thermodynamically immiscible Ag and Ni metals formed alloy nanoparticles of various compositions due to the nanosize effect. The as-synthesized alloy NPs were ~19 nm in diameter and *fcc* in crystal structure.

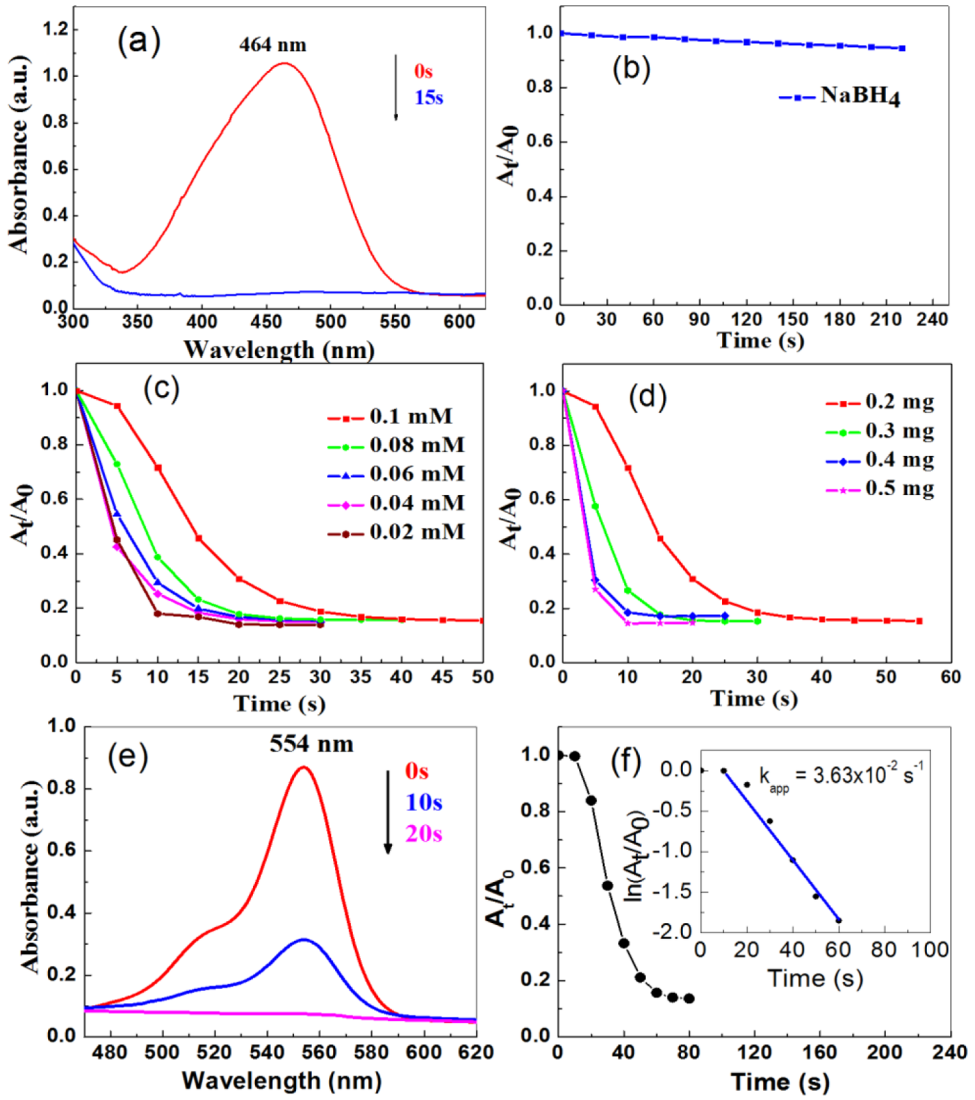

Figure 9. UV−vis absorption spectra of degradation of (a) 0.02 mM methyl orange by $NaBH_4$ in the presence of 0.2 mg of $Ag_{0.6}Ni_{0.4}$ NPs. (b) Plot of A_t/A_0 vs reaction time for a mixture of methyl orange and $NaBH_4$ without the addition of catalyst. Plots of A_t/A_0 vs reaction time for first-order kinetics (c) with varying concentration of methyl orange (0.02−0.1 mM) and constant amount (0.2 mg) of catalyst, (d) with varying amount of catalyst (0.2−0.5 mg), and constant amount (0.1 mM) of methyl orange dye. (e) UV−vis spectra of degradation of 0.02 mM RhB in the presence of 0.2 mg catalyst. (f) Plot of A_t/A_0 against time for first-order kinetics. Inset: linear plot of $\ln(A_t/A_0)$ vs time evaluating the rate constant of the RhB degradation reaction.

Table 4. Summary of Reaction Time (s), Apparent Rate Constant (k_{app}) and Activity Parameter (K) for Degradation of MO with Varying Concentration and Catalytic Loading

concentration of MO (mM)	amount of catalyst (mg)	reaction time (s)	apparent rate constant (k_{app}, 10^{-3} s^{-1})	activity parameter (K, s^{-1} g^{-1})
0.02	0.2	15	115	576.6
0.04	0.2	20	108	543.0
0.06	0.2	25	96	480.3
0.08	0.2	30	75	377.6
0.1	0.2	45	43	218.1
0.1	0.3	25	105	350.4
0.1	0.4	15	152	382.1
0.1	0.5	10	227	454.6

Apart from HRTEM and EDAX analyses, powder XRD patterns showed clearly the formation of an alloy and the incorporation of the smaller Ni atom in the bigger *fcc*-Ag crystal lattice. A systematic trend of the variation of lattice parameter or *d*-spacing of $Ag_{1-x}Ni_x$ NPs was observed according to Vegard's law with the change of "*x*". 5-Fold twinning is observed in most of the alloy NPs, confirming the presence of twinned defect sites and a highly active surface, which are mandatory for a good catalyst.

As a first case with these AgNi alloy NPs, we have carried out four catalytic reactions. All four reactions were accelerated by the present catalyst in such a way that, in all cases, we have observed accountably a very high apparent rate constant and activity parameter. These overwhelming catalytic activities of the present catalyst are due to its size, presence of twinned defect (responsible for enhanced adsorption of substrate molecules), and redox potential difference between Ag and Ni. Elaborating the last point, the electronegativity difference between the Ag and Ni metals would cause electron transfer from Ni to Ag, which finally results in the enhanced electron

transfer from reducing BH_4^- to a nitro-aromatic compound or organic dyes.

■ ASSOCIATED CONTENT

Supporting Information

Magnified XRD patterns of $Ag_{1-x}Ni_x$ nanoparticles, histograms of particle size distribution, additional HRTEM images of twinned nanostructures, and EDAX analyses. This material is available free of charge via the Internet at http://pubs.acs.org.

■ AUTHOR INFORMATION

Corresponding Author

*S. Deka. Fax: (+) 91-11-27667206. E-mail: sdeka@chemistry.du.ac.in, ssdeka@gmail.com.

Notes

The authors declare no competing financial interest.

■ ACKNOWLEDGMENTS

M.K. thanks CSIR-India for research fellowship. S.D. gratefully acknowledges the financial support received from SERB-DST (SR/S1/IC-27/2011), DAE-BRNS (2011/20/37P/11/BRNS/1733) and University of Delhi. We thank SAIF-AIIMS and USIC, DU for instrumentation facility. The authors are grateful to Ms. Mona Mittal, Chemistry Department, Indian Institute of Technology, New Delhi for useful discussions on X-ray photoelectron spectroscopy data.

■ REFERENCES

(1) Sankar, M.; Dimitratos, N.; Miedziak, P. J.; Wells, P. P.; Kielye, C. J.; Hutchings, G. J. Designing Bimetallic Catalysts for a Green and Sustainable Future. *Chem. Soc. Rev.* **2012**, *41*, 8099−8139.

(2) Singh, A. K.; Xu, Q. Synergistic Catalysis over Bimetallic Alloy Nanoparticles. *ChemCatChem* **2013**, *5*, 652−676.

(3) You, H.; Yang, S.; Dinga, B.; Yang, H. Synthesis of Colloidal Metal and Metal Alloy Nanoparticles for Electrochemical Energy Applications. *Chem. Soc. Rev.* **2013**, *42*, 2880−2904.

(4) Shankar, S.; Deka, S. Metal Nanocrystals and Their Applications in Biomedical Systems. *Sci. Adv. Mater.* **2011**, *3*, 169−195.

(5) Zhang, Z.; Nenoff, T. M.; Huang, J. Y.; Berry, D. T.; Provencio, P. P. Room Temperature Synthesis of Thermally Immiscible Ag-Ni Nanoalloys. *J. Phys. Chem. C* **2009**, *113*, 1155−1159.

(6) Zhang, Z.; Nenoff, T. M.; Leung, K.; Ferreira, S. R.; Huang, J. Y.; Berry, D. T.; Provencio, P. P.; Stumpf, R. Room-Temperature Synthesis of Ag-Ni and Pd-Ni Alloy Nanoparticles. *J. Phys. Chem. C* **2010**, *114*, 14309−14318.

(7) Gaudry, M.; Cottancin, E.; Pellarin, M.; Lerme, J.; Arnaud, L.; Huntzinger, J. R.; Vialle, J. L.; Broyer, M.; Rousset, J. L.; Treilleux, M.; Melinon, P. Size and Composition Dependence in the Optical Properties of Mixed (Transition Metal/Noble Metal) Embedded Clusters. *Phys. Rev. B* **2003**, *67*, 155409.

(8) Duan, S.; Wang, R. Bimetallic Nanostructures with Magnetic and Noble Metals and Their Physicochemical Applications. *Prog. Nat. Sci.* **2013**, *23*, 113−126.

(9) Lin, S. C.; Chen, S. Y.; Chen, Y. T.; Cheng, S. Y. Electrochemical Fabrication and Magnetic Properties of Highly Ordered Silver−Nickel Core-Shell Nanowires. *J. Alloys Compd.* **2008**, *449*, 232−236.

(10) Guo, J.; Wang, X.; Miao, P.; Liao, X.; Zhanga, W.; Shi, B. One-Step Seeding Growth of Controllable Ag@Ni Core−Shell Nanoparticles on Skin Collagen Fiber with Introduction of Plant Tannin and their Application in High-Performance Microwave Absorption. *J. Mater. Chem.* **2012**, *22*, 11933−11942.

(11) Gawande, M. B.; Guo, H.; Rathi, A. K.; Branco, P. S.; Chen, Y.; Varmad, R. S.; Peng, D. L. First Application of Core-Shell Ag@Ni Magnetic Nanocatalyst for Transfer Hydrogenation Reactions of Aromatic Nitro and Carbonyl Compounds. *RSC Adv.* **2013**, *3*, 1050−1054.

(12) Senapati, S.; Srivastava, S. K.; Singh, S. B.; Mishra, H. N. Magnetic Ni/Ag Core−Shell Nanostructure from Prickly Ni Nanowire Precursor and its Catalytic and Antibacterial Activity. *J. Mater. Chem.* **2012**, *22*, 6899−6906.

(13) Xiao, S.; Hua, W.; Luo, W.; Wu, Y.; Li, X.; Deng, H. Size Effect on Alloying Ability and Phase Stability of Immiscible Bimetallic Nanoparticles. *Eur. Phys. J. B* **2006**, *54*, 479−484.

(14) Ma, E. Alloys Created Between Immiscible Elements. *Prog. Mater. Sci.* **2005**, *50*, 413−509.

(15) Tung, C. Y.; Gu, J. M.; Lin, H. M.; Hwu, Y.; Cheng, N. F. X-ray Absorption Spectroscopy Study of Ag_XNi_{1-x} Nanocrystalline Solid Solutions. *Nanostruct. Mater.* **1997**, *9*, 351−354.

(16) Srivastava, C.; Chithra, S.; Malviya, K. D.; Sinha, S. K.; Chattopadhyay, K. Size Dependent Microstructure for Ag−Ni Nanoparticles. *Acta Mater.* **2011**, *59*, 6501−6509.

(17) Santhi, K.; Thirumal, E.; Karthick, S. N.; Kim, H. J.; Nidhin, M.; Narayanan, V.; Stephen, A. Synthesis, Structure Stability and Magnetic Properties of Nanocrystalline Ag−Ni Alloy. *J. Nanopart. Res.* **2012**, *14*, 868.

(18) Sridharan, K.; Endo, T.; Cho, S. G.; Kim, J.; Park, T. J.; Philip, R. Single Step Synthesis and Optical Limiting Properties of Ni−Ag and Fe−Ag Bimetallic Nanoparticles. *Opt. Mater.* **2013**, *35*, 860−867.

(19) Saha, S.; Pal, A.; Kundu, S.; Basu, S.; Pal, T. Photochemical Green Synthesis of Calcium-Alginate-Stabilized Ag and Au Nanoparticles and Their Catalytic Application to 4-Nitrophenol Reduction. *Langmuir* **2010**, *26*, 2885−2893.

(20) Gupta, V. K.; Yola, M. L.; Eren, T.; Kartal, F.; Çağlayan, M. O.; Atar, N. Catalytic Activity of Fe@Ag Nanoparticle Involved Calcium Alginate Beads for the Reduction of Nitrophenols. *J. Mol. Liq.* **2014**, *190*, 133−138.

(21) Zeng, T.; Ziegelgruber, K. L.; Chin, Y. P.; Arnold, W. A. Pesticide Processing Potential in Prairie Pothole Porewaters. *Environ. Sci. Technol.* **2011**, *45*, 6814−6822.

(22) Megharaj, M.; Pearson, H. W.; Venkateswarlu, K. Toxicity of Phenol and Three Nitrophenols towards Growth and Metabolic Activities of Nostoc Linckia, Isolated from Soil. *Arch. Environ. Contam. Toxicol.* **1991**, *21*, 578−584.

(23) Li, X.; Wang, X.; Song, S.; Liu, D.; Zhang, H. Selectively Deposited Noble Metal Nanoparticles on Fe_3O_4/Graphene Composites: Stable, Recyclable, and Magnetically Separable Catalysts. *Chem.—Eur. J.* **2012**, *18*, 7601−7607.

(24) Fu, H.; Yang, X.; Jiang, X.; Yu, A. Bimetallic Ag−Au Nanowires: Synthesis, Growth Mechanism, and Catalytic Properties. *Langmuir* **2013**, *29*, 7134−7142.

(25) Yang, J.; Shen, X.; Zhu, G.; Ji, Z.; Zhou, H. ZnNi Alloy Nanoparticles Grown on Reduced Graphene Oxide Nanosheets and their Magnetic and Catalytic Properties. *RSC Adv.* **2014**, *4*, 386−394.

(26) Zhang, J.; Chen, G.; Guay, D.; Chaker, M.; Ma, D. Highly Active PtAu Alloy Nanoparticle Catalysts for the Reduction of 4-Nitropheno. *Nanoscale* **2014**, *6*, 2125−2130.

(27) Peng, Y.; Wu, X.; Qiu, L.; Liu, C.; Wang, S.; Yan, F. Synthesis of Carbon−PtAu Nanoparticle Hybrids Originating from Triethoxysilane-Derivatized Ionic Liquids for Methanol Electrooxidation and the Catalytic Reduction of 4-Nitropheno. *J. Mater. Chem. A* **2013**, *1*, 9257−9263.

(28) Wu, K. L.; Wei, X. W.; Zhou, X. M.; Wu, D. H.; Liu, X. W.; Ye, Y.; Wang, Q. $NiCo_2$ Alloys: Controllable Synthesis, Magnetic Properties, and Catalytic Applications in Reduction of 4-Nitrophenol. *J. Phys. Chem. C* **2011**, *115*, 16268−16274.

(29) Bai, S.; Shen, X.; Zhu, G.; Li, M.; Xi, H.; Chen, K. In situ Growth of Ni_xCo_{100-x} Nanoparticles on Reduced Graphene Oxide Nanosheets and Their Magnetic and Catalytic Properties. *ACS Appl. Mater. Interfaces* **2012**, *4*, 2378−2386.

(30) Carenco, S.; Boissiere, C.; Nicole, L.; Sanchez, C.; Floch, P. L.; Mezailles, N. Controlled Design of Size-Tunable Monodisperse Nickel Nanoparticles. *Chem. Mater.* **2010**, *22*, 1340−1349.

(31) Lee, C.-C.; Chen, D.-H. Large-Scale Synthesis of Ni−Ag Core−Shell Nanoparticles with Magnetic, Optical and Anti-Oxidation Properties. *Nanotechnology* **2006**, *17*, 3094−3099.

(32) Chen, D.-H.; Hsieh, C.-H. Synthesis of Nickel Nanoparticles in Aqueous Cationic Surfactant Solutions. *J. Mater. Chem.* **2002**, *12*, 2412−2415.
(33) Wu, S.-H.; Chen, D.-H. Synthesis and Characterization of Nickel Nanoparticles by Hydrazine Reduction in Ethylene Glycol. *J. Colloid Interface Sci.* **2003**, *259*, 282−286.
(34) Lee, C. C.; Cheng, Y. Y.; Chang, H. Y.; Chen, D. H. Synthesis and Electromagnetic Wave Absorption Property of Ni−Ag Alloy Nanoparticles. *J. Alloys Compd.* **2009**, *480*, 674−680.
(35) Tsen, S. C. Y.; Crozier, P. A.; Liu, J. Lattice Measurement and Alloy Compositions in Metal and Bimetallic Nanoparticles. *Ultramicroscopy* **2003**, *98*, 63−72.
(36) Hofmeister, H. High-Resolution Electron Microscopy Studies of Metal Nanoparticles: Shape and Twin Defects, and Surface Stress Effects. *J. Optoelectron. Adv. Mater.* **2007**, *9*, 99−105.
(37) Tao, A. R.; Habas, S.; Yang, P. Shape Control of Colloidal Metal Nanocrystals. *Small* **2008**, *4*, 310−325.
(38) Elechiguerra, J. L.; Reyes-Gasgab, J.; Yacaman, M. J. The Role of Twinning in Shape Evolution of Anisotropic Noble Metal Nanostructures. *J. Mater. Chem.* **2006**, *16*, 3906−3919.
(39) Lu, D.l.; Domen, K.; Tanaka, K. I. Electrodeposited Au−Fe, Au−Ni, and Au−Co Alloy Nanoparticles from Aqueous Electrolytes. *Langmuir* **2002**, *18*, 3226−3232.
(40) Prieto, P.; Nistor, V.; Nouneh, K.; Oyama, M.; Abd-Lefdil, M.; Díaz, R. XPS Study of Silver, Nickel and Bimetallic Silver−Nickel Nanoparticles Prepared by Seed-Mediated Growth. *Appl. Surf. Sci.* **2012**, *258*, 8807−8813.
(41) Grosvenor, A. P.; Biesinger, M. C.; Smart, R. St.C. N.; McIntyre, S. New Interpretations of XPS Spectra of Nickel Metal and Oxides. *Surf. Sci.* **2006**, *600*, 1771−1779.
(42) Huang, J.; Vongehr, S.; Tang, S.; Lu, H.; Meng, X. Highly Catalytic Pd−Ag Bimetallic Dendrites. *J. Phys. Chem. C* **2010**, *114*, 15005−15010.
(43) An, Q.; Yu, M.; Zhang, Y.; Ma, W.; Guo, J.; Wang, C. Fe_3O_4@Carbon Microsphere Supported Ag−Au Bimetallic Nanocrystals with the Enhanced Catalytic Activity and Selectivity for the Reduction of Nitroaromatic Compounds. *J. Phys. Chem. C* **2012**, *116*, 22432−22440.
(44) Zhang, P.; Li, R.; Huang, Y.; Chen, Q. A Novel Approach for the in Situ Synthesis of Pt−Pd Nanoalloys Supported on Fe_3O_4@C Core−Shell Nanoparticles with Enhanced Catalytic Activity for Reduction Reactions. *ACS Appl. Mater. Interfaces* **2014**, *6*, 2671−2678.
(45) Zhang, Z.; Shao, C.; Zou, P.; Zhang, P.; Zhang, M.; Mu, J.; Guo, Z.; Li, X.; Wang, C.; Liu, Y. In Situ Assembly of Well-Dispersed Gold Nanoparticles on Electrospun Silica Nanotubes for Catalytic Reduction of 4-Nitrophenol. *Chem. Commun.* **2011**, *47*, 3906−3908.
(46) Wang, D.; Peng, Q.; Li, Y. Nanocrystalline Intermetallics and Alloys. *Nano Res.* **2010**, *3*, 574−580.
(47) Rajesh, R.; Kumar, S. S.; Venkatesan, R. Efficient Degradation of Azo Dyes Using Ag and Au Nanoparticles Stabilized on Graphene Oxide Functionalized with PAMAM Dendrimers. *New J. Chem.* **2014**, *38*, 1551−1558.
(48) Xu, D.; Cheng, F.; Lu, Q.; Dai, P. Microwave Enhanced Catalytic Degradation of Methyl Orange in Aqueous Solution over CuO/CeO_2 Catalyst in the Absence and Presence of H_2O_2. *Ind. Eng. Chem. Res.* **2014**, *53*, 2625−2632.